J. Appl. Comput. Mech., 11(2) (2025) 502-518
DOI: 10.22055/jacm.2024.46917.4624

ISSN: 2383-4536
jacm.scu.ac.ir

Shahid Chamran University of Ahvaz

Journal of Applied and Computational Mechanics

Research Paper

Numerical Analysis of Preheating Furnace Performance in Razi Petrochemical's Ammonia Processing Unit Considering the Effects of Hydraulic and Geometric Variables

Alireza Daneh-Dezfuli, Shiva Khamisi, Seyed Saied Bahrainian

Department of Mechanical Engineering, Faculty of Engineering, Shahid Chamran University of Ahvaz, Ahvaz, Iran,
Email: a.danehdezfuli@scu.ac.ir (A.D.D.); khamisishiva@yahoo.com (S.Kh.); Bahrainian@scu.ac.ir (S.S.B.)

Received May 15 2024; Revised August 31 2024; Accepted for publication August 31 2024.
Corresponding author: A. Daneh-Dezfuli (a.danehdezfuli@scu.ac.ir)

Abstract. This study investigates the combustion of natural gas within a three-dimensional preheating ammonia furnace at the Razi Petrochemical Company (RPC) in Mahshahr, Iran. The furnace geometry is modeled assuming non-premixed fuel and air. We present a model of steady-state compressible chemical-turbulence combustion, incorporating conductive, convective, and radiative heat transfers. Zeldovich and Fenimore mechanisms are utilized to address thermal and prompt pollutant emissions in the presented computational fluid dynamics (CFD) simulations. Furnace performance was evaluated based on hydraulic parameters and geometric parameters. Results indicate that excess air (inverse of equivalence ratio) significantly influences combustion within the furnace. For instance, pollutant emissions increase by 50.62%, 53.27%, and 56.2%, respectively with the addition of 20%, 40%, and 60% excess air at a constant fuel mass flow rate of 0.0557 kg/s.

Keywords: Combustion Process; Preheating Ammonia Furnace; Razi Petrochemical Company.

1. Introduction

In today's world, a significant portion of energy production relies on burning gaseous fuels like methane, ethane, and ethylene. Stricter regulations on combustion pollutants have spurred a critical need for designing more efficient combustion systems. Numerical simulation stands out as a key technique for analyzing furnace performance, aiming to attain optimal process conditions, lower fuel consumption, enhance heat transfer rates, and minimize pollutants [1, 2]. This applied research focuses on investigating the performance of RPC's ammonia preheating furnace, taking into account the influence of hydraulic and geometric parameters.

Extensive research efforts have been devoted to numerically analyzing the performance of combustion furnaces. Previous studies have explored various methods for modeling nitrogen oxides and comparing them with experimental data Mancini et al. [3]. While discrepancies were observed in fuel jet areas, satisfactory predictions were obtained for species mass fractions and pollutant emissions in other regions. Additionally, investigations into the impact of different equivalence ratios and fuel mass flows on methane-air combustion processes have revealed significant temperature gradients along the burner centerline Yapıcı et al. [4]. Furthermore, numerical modeling of heavy oil fuel combustion in laboratory furnaces underscored the dependence of predicted results on turbulence, chemistry, combustion models, numerical schemes, and boundary conditions Saario et al. [5]. Similarly, analyses of propane combustion in cross-flowing streams of preheated, oxygen-deficient air highlighted the influence of fuel temperature on flame size Yang and Blasiak [6]. Studies on wall-fired furnaces using commercial codes like FLUENT indicated the significant impact of excess air on furnace temperatures Vuthaluru and Vuthaluru [7]. Additionally, CFD-based simulations have been employed to optimize the shape of pulverized coal-fired boilers, emphasizing the importance of combustion air stream momentum for efficient boiler performance Schaffel-Mancini et al. [8]. Exploring Moderate or Intense Low-oxygen Dilution (MILD) combustion, researchers found that increasing fuel injection velocity enhances fuel-oxidizer mixing Huang et al. [9]. Interpretations of methane MILD combustion characteristics using computational modules like OPPDIF from the CHEMKIN package have shed light on combustion dynamics He et al. [10]. Moreover, investigations into the effect of excess air on combustion dynamics in vertical furnaces demonstrated the utility of CFD as a predictive tool for combustion specifications Elorf and Sarh [11]. Finally, CFD numerical studies of propane combustion in laboratory-scale cylindrical furnaces highlighted the advantages of the standard k-ε turbulence model over its realizable form in combustion simulations Tu et al. [12].

Ceglie et al. [13] investigated the behavior of a burner using methane-air and hydrogen-air mixtures. This study utilized CFD simulations to analyze the stability of the combustion process. The results indicated that hydrogen-air mixtures lead to greater instability compared to methane-air mixtures, due to changes in flame topology, heat release rates, and time delays. The research emphasizes the importance of understanding these parameters for the development of next-generation hydrogen burners aimed at efficient and stable energy production.

Cao et al. [14] studied the combustion characteristics of a premixed methane-air mixture in a porous media burner (PMB) designed to optimize performance for residential gas water heaters (GWH). Experimental and numerical approaches have been combined to assess flame stability, temperature profiles, and pollutant emissions, using ANSYS Fluent for numerical modeling. The results, validated against experimental data, highlighted key findings, including optimizing pore size and porosity to enhance flame stability and reduce NOx emissions. The obtained findings demonstrated that a well-optimized porous media structure could significantly improve combustion efficiency and reduce emissions, making it a promising technology for residential heating applications.

Sun et al. [15] conducted a numerical investigation into the flow and flame structures of an industrial swirling inverse diffusion methane/air burner, focusing on the effects of burner configuration on combustion performance. Turbulent flow and combustion characteristics have been captured using the Reynolds-Averaged Navier-Stokes (RANS) method and simplified reaction mechanisms. The reported results showed that the swirl motion creates a central recirculation zone and two external recirculation zones, which enhance flame stability. Additionally, it is reported that adjusting the number of fuel nozzles was more effective in reducing NOx emissions than altering the inclination angle of the nozzles. The optimal configuration involved 16 fuel nozzles at a 60° inclination angle, resulting in a significant 28.5% reduction in NOx emissions compared to the reference condition.

Dekhatawala et al. [16] examined the effects of the equivalence ratio (ϕ) on flame morphology, thermal characteristics, and emissions in an inverse diffusion porous (IDP) burner. Both experimental and computational methods have been used to evaluate the impact of different ϕ values on flame structure and pollutant emissions, particularly NOx and CO. The findings indicated that the presence of a porous medium significantly affects flame shape and stability, leading to reduced emissions at specific equivalence ratios. The study suggests that optimizing the equivalence ratio and the properties of the porous medium can improve burner performance, making it more suitable for clean combustion applications.

Liao et al. [17] conducted a numerical simulation study on MILD oxy-fuel combustion, with an emphasis on CO_2 capture and storage. This research explored the performance of a 200 MWe coal-fired boiler using advanced combustion techniques. The study focused on increasing thermal efficiency while minimizing CO_2 emissions. The results showed that integrating CO_2 capture with oxy-fuel combustion could significantly reduce greenhouse gas emissions. Additionally, they discussed the challenges associated with the large-scale implementation of this technology and provided insights into optimizing combustion processes for improved environmental performance.

Hulsbos et al. [18] investigated the combustion characteristics of hybrid iron-methane-air flames using a novel burner designed with the Heat Flux Method (HFM). This study measured the burning velocity of hybrid flames, focusing on the effects of adding iron powder to stoichiometric methane-air mixtures. The results showed a steady decrease in burning velocity with increased iron concentration, and these findings were validated through 1D simulations. It has been also addressed the uncertainties related to iron mass flow stability, which influences flame propagation. The research highlighted the potential of metal powder combustion for clean energy storage and CO_2 emission reduction.

Füzesi et al. [19] conducted a CFD study on the combustion of ammonia-methane mixtures in a swirl burner using the Flamelet Generated Manifold (FGM) model. The presented research focused on simulating chemical conversion and flow fields while considering the effects of varying ammonia concentrations. The results showed that increasing ammonia content leads to reduced flame stability and higher NOx emissions. It emphasized the necessity of carefully optimizing burner design and operating conditions to balance combustion efficiency and emission control when using ammonia-methane mixtures as fuel.

Al-Khafaji et al. [20] examined the combustion characteristics of ammonia in a swirl burner using experimental and numerical methods. It analyzed the influence of ammonia concentration on flame stability and emission levels, particularly NOx. The results embraced that ammonia combustion poses significant challenges in achieving stable and efficient burning with low emissions. The study proposed strategies for optimizing burner design to mitigate these challenges, emphasizing the potential of ammonia as a carbon-free fuel for industrial applications, despite difficulties in managing NOx emissions and maintaining flame stability.

This study advances furnace performance optimization at Razi Petrochemical's Ammonia Unit by combining detailed 3D simulations of turbulence-chemistry interactions with a focused analysis of hydraulic and geometric parameters affecting Furnace 102B. By assessing the impact of four key parameters—equivalence ratio, fuel mass flow, and the hydrodynamic diameters of air and fuel nozzles this research tailors improvements to meet the unique design and operational challenges of the furnace, which features a distinctive spiral coil structure. The simulations, conducted in a comprehensive 3D environment, enable an accurate representation of the combustion process, including conductive, convective, and radiative heat transfers using a mix of fuel (CH_4) and air (O_2 and N_2) as non-premixed gases. This study also innovatively applies Zeldovich and Fenimore mechanisms to effectively manage NOx emissions, addressing both thermal and prompt emission pathways, while investigating critical issues like hot spots through detailed thermal analyses. The combined approach not only boosts efficiency and environmental compliance but also enhances the durability and safety of furnace operations, making significant contributions to industrial practices in energy optimization and emission reduction.

2. Geometrical Modeling

The main components of RPC's furnace comprise the shell, spiral coil, and burner, as depicted in Fig. 1(a). The shell body consists of the spiral coil, conic section, and exhaust segment. Figure 1(b) illustrates the flow of ammonia vapor through the spiral tube from numbered circles 1 to 2. Non-premixed fuel and air are injected into the shell along the furnace centerline (Y-axis direction) from circles numbered 3 and 4, respectively. Combustion products exit from the shell outlet marked by the circle labeled with the number 5. Detailed dimensions of the different parts are provided in Table 1.

The fuel and air nozzle diameters, highlighted in Table 1, are two geometric parameters whose effects on furnace performance are investigated in this study. Due to the asymmetry of the furnace, its geometry is modeled in 3D space using SpaceClaim solid modeling software, available in the ANSYS 2019 R2 release. Initially, the spiral coil was prepared using Computer-Aided-Design (CAD) techniques, as depicted in Fig. 2(a). Subsequently, by combining the shell volume with the spiral coil, the furnace geometry was finalized in Fig. 2(b), incorporating all necessary geometrical features.

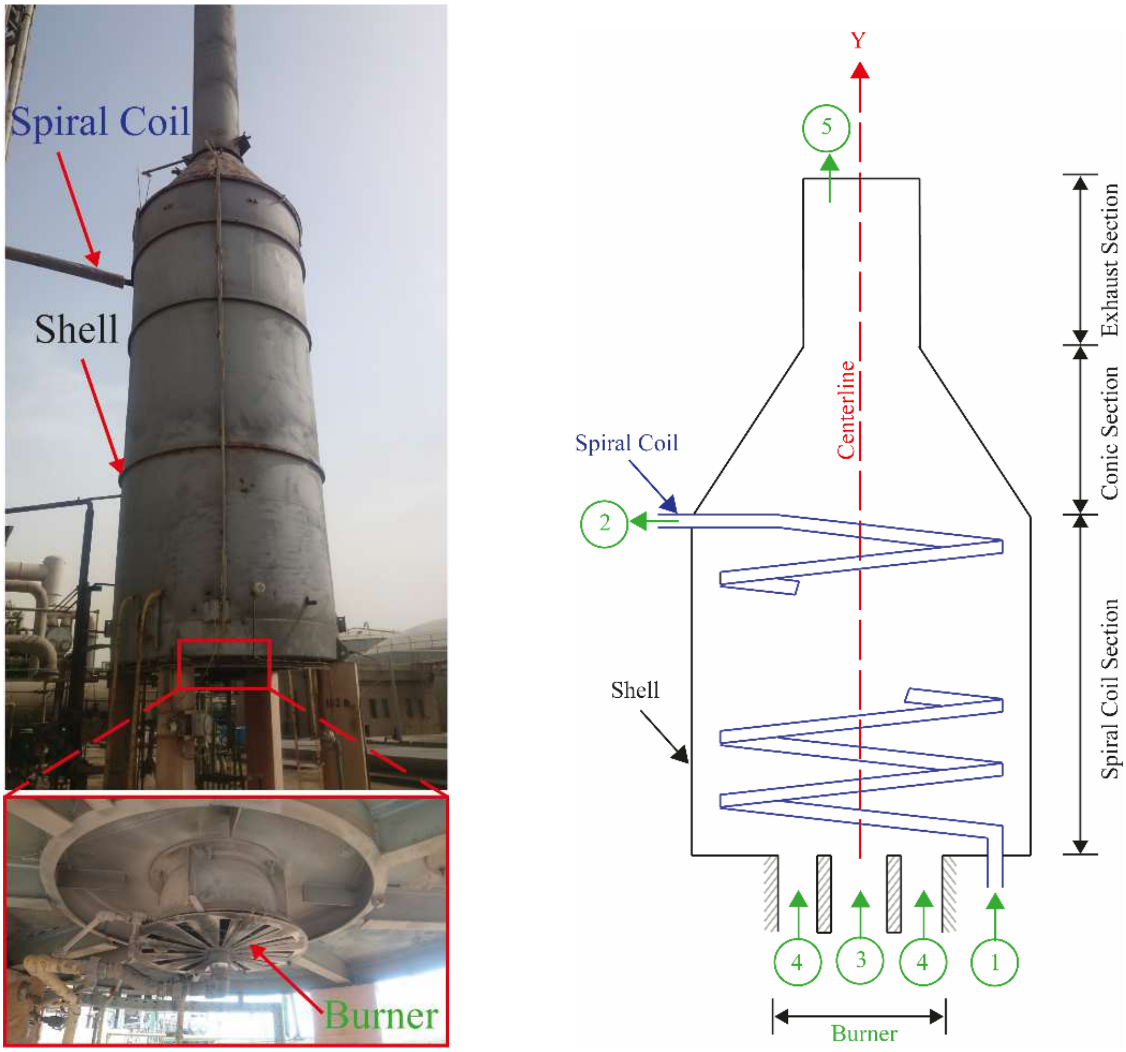

(a) (b)

Fig. 1. Representation of the RPC's ammonia preheating furnace, (a) Realistic exhibition (b) Schematic view (①,②: Ammonia vapor through the spiral tube, ③,④: Non-premixed fuel and air are injected into the shell, ⑤: Shell outlet).

3. Mathematical Modeling

The mathematical modeling of the combustion process inside the furnace involves solving conservation equations for a steady, 3D asymmetric, turbulent, and compressible multi-species fluid flow. The assumption of an ideal gas is applied to calculate the thermal properties of the mixture. Turbulent flow is accounted for using the standard k-ε turbulence model. For chemical species transport and reacting flow, the eddy dissipation model is utilized. Additionally, the thickness of the burner parts is neglected in the model.

Table 1. RPC furnace's geometrical dimensions.

Description	Symbol	Value
Shell		
Diameter of burner-side surface	d_{bs}	3 m
Diameter of exhaust-side surface	d_{es}	1 m
Height of spiral tube section	h_{st}	6 m
Height of conic section	h_{con}	3 m
Height of exhaust section	h_{ex}	3 m
Spiral coil		
Tube interior diameter	ID	0.1524 m
Tube outside diameter	OD	0.1683 m
Number of coils	----	14
Coil outside diameter	d_t	2.7 m
Total length of spiral tube	L	124.97 m
Burner		
Fuel nozzle diameter	d_f	0.1 m
Hydraulic diameter of air nozzle	$d_{h,a}$	0.23 m

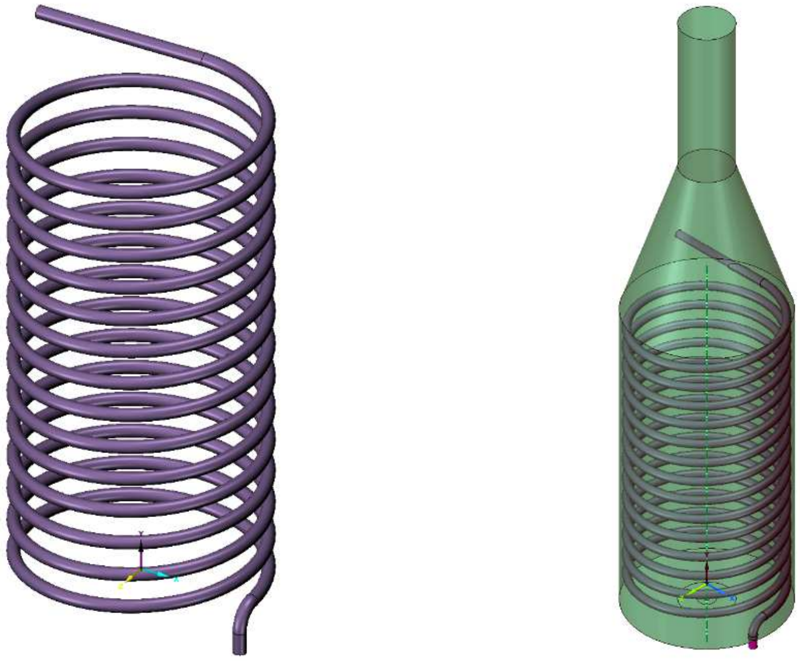

(a) (b)

Fig. 2. CAD model of the RPC's furnace, (a) Spiral coil, (b) Final geometry.

3.1. Conservation Equations

Local mass fraction of each combustion species, $Y_{i'}$, predicts through the solution of a convection-diffusion equation for the species i' as [21]:

$$\frac{\partial}{\partial x_i}(\rho u_i Y_{i'}) = -\frac{\partial}{\partial x_i} J_{i',i} + R_{i'} \tag{1}$$

where, x_i implies on coordinates in i = x, y and z directions. ρ and u_i denote density and velocity field, respectively. $R_{i'}$ is the net rate of production of species by chemical reaction. $J_{i',i}$ represents the diffusion flux of species i', which in turbulent flow arises due to gradients of concentration and temperature as:

$$J_{i',i} = -\left(\rho D_{i',mix} + \frac{\mu_t}{Sc_t}\right)\frac{\partial Y_{i'}}{\partial x_i} - D_{T,i'}\frac{1}{T}\frac{\partial T}{\partial x_i} \tag{2}$$

where, μ_t and Sc_t are turbulent viscosity and Schmidt number. T denotes temperature. $D_{T,i'}$ is thermal (Soret) diffusion coefficient for species i'. $D_{i',mix}$ is mass diffusion coefficient for species i' in mixture, mix as:

$$D_{i',mix} = \frac{1 - X_{i'}}{\sum_{j',j' \neq i'} X_{i'} / D_{i'j'}} \tag{3}$$

where, $X_{i'}$ is mole fraction for species i'. $D_{i'j'}$ is binary mass diffusion coefficient for species i' in species j'. Momentum equation can be expressed as [22]:

$$\frac{\partial}{\partial x_j}(\rho u_i u_j) = \frac{\partial (\tau_{ij})_e}{\partial x_j} - \frac{\partial p}{\partial x_i} \tag{4}$$

where, p represents pressure. $(\tau_{ij})_e$ is effective stress tensor as:

$$(\tau_{ij})_e = \mu_e\left(\frac{\partial u_i}{\partial x_j} + \frac{\partial u_j}{\partial x_i}\right) - \frac{2}{3}\mu_e\frac{\partial u_l}{\partial x_l} \tag{5}$$

Effective turbulent, $\mu_e = \mu + \mu_t$, where μ is molecular viscosity. Energy equation is described by [23]:

$$\frac{\partial}{\partial x_i}\left[u_i(\rho E + p)\right] = \frac{\partial}{\partial x_i}\left[\lambda_e\frac{\partial T}{\partial x_i} - \sum_{j'} h_{j'} J_{j'} + u_j(\tau_{ij})_e\right] + S_h \tag{6}$$

where $J_{j'}$ is the diffusion flux of species j'. S_h includes the heat of chemical reaction and radiation:

$$E = h - \frac{p}{\rho} + \frac{u_i^2}{2} \tag{7}$$

where h is sensible enthalpy as [24]:

$$h = \sum_{j'} Y_{j'} h_{j'} \tag{8}$$

where,

$$h_{j'} = \int_{T_{ref}}^{T} C_{p,j'} dT \tag{9}$$

where, $C_{p,j'}$ denotes specific heat at constant pressure of species j'. Effective conductivity λ_e is calculated as:

$$\lambda_e = \alpha C_p \mu_e \tag{10}$$

where, the inverse effective Prandtl number, α, is computed using the following formula [25]:

$$\left|\frac{\alpha - 1.3929}{\alpha_0 - 1.3929}\right|^{0.6321} \left|\frac{\alpha - 2.3929}{\alpha_0 - 2.3929}\right|^{0.3679} = \frac{\mu}{\mu_e} \tag{11}$$

where, α_0 is the inverse effective Prandtl number at reference temperature, T_{ref}.

3.2. Thermal Properties of Mixture

Density, viscosity, specific heat and thermal conductivity of mixture are calculated according to the relevant properties of mixture species based on the ideal-gas-mixing-law as follows [4]:

$$\rho = \frac{p_{op} + p}{\Re T \sum_{i'} \frac{Y_{i'}}{M_{i'}}} \tag{12}$$

$$C_p = \sum_{i'} Y_{i'} C_{p,i'} \tag{13}$$

$$\lambda = \sum_{i'} \frac{X_{i'} \lambda_{i'}}{\sum_{j'} X_{j'} \varphi_{i',j'}} \tag{14}$$

$$\mu = \sum_{i'} \frac{X_{i'} \mu_{i'}}{\sum_{j'} X_{j'} \varphi_{i',j'}} \tag{15}$$

where, $\Re$ and $M_{i'}$ represent the gas universal constant and molecular weight of species i', respectively. p_{op} is operating pressure, and:

$$\varphi_{i',j'} = \frac{\left[1 + \left(\frac{\mu_{i'}}{\mu_{j'}}\right)^{\frac{1}{2}} \left(\frac{M_{j'}}{M_{i'}}\right)^{\frac{1}{4}}\right]^2}{\left[8\left(1 + \frac{M_{i'}}{M_{j'}}\right)\right]^{\frac{1}{2}}} \tag{16}$$

3.3. Turbulence Modeling

Turbulent viscosity required for the estimation of diffusion flux and effective stress tensor can be achieved by:

$$\mu_t = \rho C_\mu \frac{k^2}{\varepsilon} \tag{17}$$

which is computed based on turbulence kinetic energy, k and dissipation rate, ε. Ignoring buoyancy forces, these turbulence parameters are calculated using the standard $k - \varepsilon$ turbulence model with the form of [26]:

$$\frac{\partial}{\partial x_i}(\rho u_i k) = \frac{\partial}{\partial x_j}\left[\left(\mu + \frac{\mu_t}{\sigma_k}\right)\frac{\partial k}{\partial x_j}\right] + G_k - \rho\varepsilon \tag{18}$$

$$\frac{\partial}{\partial x_i}(\rho u_i \varepsilon) = \frac{\partial}{\partial x_j}\left[\left(\mu + \frac{\mu_t}{\sigma_\varepsilon}\right)\frac{\partial \varepsilon}{\partial x_j}\right] + C_1 \frac{\varepsilon}{k} G_k - C_2 \rho \frac{\varepsilon^2}{k} \tag{19}$$

where,

$$G_k = \mu_t \left(\frac{\partial u_i}{\partial x_j} + \frac{\partial u_j}{\partial x_i}\right)\frac{\partial u_i}{\partial x_i} \tag{20}$$

The values of constant coefficients, C_μ, C_1, C_2, σ_k and σ_ε are 0.09, 1.44, 1.92, 1.0 and 1.3, respectively.

3.4. Radiation Modeling

Radiation heat transfer, which is the dominant factor in furnaces operation, has been taken into account by the Discrete Ordinates (DO) model [27]. This model considers radiative transfer equation that can be written for spectral intensity $I_\lambda(r,s)$ as:

$$\nabla.\left(I_\lambda(r,s)s\right)+(a_\lambda+\sigma_s)I_\lambda(r,s)=a_\lambda n^2 I_{b\lambda}+\frac{\sigma_s}{4\pi}\int_0^{4\pi}I_\lambda(r,s')\Phi(s,s')d\Omega' \tag{21}$$

where, λ is wavelength. r, s and s' are the position vector, direction vector and scattering direction vector, respectively. $I_{b\lambda}$ is black body intensity given by the Planck function, $\Phi(s,s')$, which is the scattering phase function. a_λ denotes spectral absorption coefficient. n represents refractive index. σ_s is Stefan's constant. Ω' is space angle.

3.5. Combustion of Fuel with Air

Reaction mechanism of fuel with stoichiometric air (ideal mass of air required to completely burn all of the fuel) is defined by [4]:

$$2(O_2+3.76N_2)\Rightarrow CO_2+2H_2O+7.52N_2 \tag{22}$$

If the quantity of air available for combustion is greater than the ideal quantity for complete oxidation of the fuel, then a lean mixture occurs. The equation for combustion of a lean mixture is:

$$CH_4+\frac{2}{\phi}(O_2+3.76N_2)\Rightarrow CO_2+2H_2O+2\left(\frac{1-\phi}{\phi}\right)O_2+\frac{7.52}{\phi}N_2 \tag{23}$$

where ϕ is called the equivalence ratio, defined as the stoichiometric air/fuel ratio, AFR_{sto} divided by actual air/fuel ratio, AFR_{act}, i.e.:

$$\phi=\frac{AFR_{sto}}{AFR_{act}} \tag{24}$$

where,

$$AFR=\frac{\dot{m}_{air}}{\dot{m}_f} \tag{25}$$

where $\dot{m}_{air}$ and $\dot{m}_f$ are the mass flow of air and fuel, respectively. The air excess ratio is the reciprocal of the equivalence ratio. Two incomplete combustion mechanisms are used here. The first mechanism is in associated with the combustion in high temperatures that nitrogen of air can react with oxygen to form NO_2 and NO. This process is modeled by the Zeldovich mechanism [28]. The second mechanism is related to the formation of nitrogen oxides when not enough time for fuel and air is provided for proper combustion. The Fenimore prompt mechanism is employed to model the second incomplete combustion [28].

3.6. Modeling of Species Production Rate

The eddy dissipation model [27] is utilized to evaluate the rate of species production. The output of this model is required to assess source term in Eq. (1). The source of chemical species i' due to reaction, $R_{i'}$, is computed as the sum of reaction sources over N_R reactions in which the species may participate:

$$R_{i'}=M_{i'}\sum_{l=1}^{N_R}R_{i',l} \tag{26}$$

where $R_{i',l}$ is the molar rate of creation/destruction of species i' in reaction l. This term is given by the smaller of the two expressions (reactant dissipation and product dissipation) as follows:

$$R_{i',l}=\min\left\{\underbrace{\upsilon'_{i',l}M_{i'}A\rho\frac{\varepsilon}{k}\frac{Y_R}{\upsilon'_{R,l}M_R}}_{\text{Reaction dissipation}},\underbrace{\upsilon'_{i',l}M_{i'}AB\rho\frac{\varepsilon}{k}\frac{\sum_P Y_P}{\sum_{j'}^{N}\upsilon''_{j',l}M_{j'}}}_{\text{Product dissipation}}\right\} \tag{27}$$

where $\upsilon'_{i',l}$ is the stoichiometric coefficient for reactant i' in reaction l. $\upsilon''_{j',l}$ is the stoichiometric coefficient for product j' in reaction l. Y_P represents the mass fraction of any product species P. Y_R represents the mass fraction of a particular reactant R (R is the reactant species giving the smallest value of $R_{i',l}$). A and B are empirical constants equal to 4.0 and 0.5, respectively. The eddy dissipation model relates the rate of reaction to the rate of dissipation of the reactant and product containing eddies. k/ε represents the time scale of the turbulent eddies following the eddy dissipation model of Spalding [4].

4. Simulation Methodology

The aforementioned mathematical equations outlined in the previous section are solved using the finite-volume (FV) numerical method available in ANSYS-FLUENT 2019 R2 release. This paper utilized a reduced kinetic scheme for methane-based flames provided by ANSYS Fluent, which balances accuracy and computational efficiency, making it suitable for large-scale industrial simulations. This scheme focuses on key species such as CH_4, O_2, CO, CO_2, H_2O, and important radicals, involving primary reactions like methane oxidation. ANSYS Fluent supports both non-premixed and premixed combustion models, offering detailed and reduced mechanisms to simplify kinetics and reduce computational load. The software's advanced capabilities include pollutant prediction models, various radiation models, and effective turbulence-chemistry interaction modeling. These features enable accurate simulations of flame behavior and pollutant formation, facilitating comprehensive analyses, optimized designs, and improved operational strategies for industrial combustion systems. To this end, the operating conditions of the RPC furnace, serving as hydraulic and thermal boundary conditions (BCs), are presented in Table 2. In Table 2, it can be observed that ammonia vapor enters the coil at a mass flow rate of 2.05 kg/s and a temperature of 524.82 K. Due to the lack of pressure information, the same mass flow rate is maintained at the coil outlet.

Table 2. RPC furnace's operating condition based on Fig. 1(b) notations.

Circle No.	Description	Hydraulic BC	Thermal BC
1	Ammonia inlet	Mass flow of 2.05 kg/s	524.82 K
2	Ammonia outlet	Mass flow of 2.05 kg/s	NR*
3	Fuel	Mass flow of 0.0557 kg/s	300 K
4	Air	Mass flow of 1.15 kg/s ($\phi = 0.833$)	300 K
5	Exhaust	Atmospheric pressure	NR

* NR: not required

Table 3. Specifications of steel used in the spiral coil.

ρ (kg/m^3)	C_p (J/kg.K)	λ (W/m.K)
8030	502.48	16.27

Both fuel and air are injected into the furnace at a temperature of 300 K, with mass flow rates of 0.0557 kg/s and 1.15 kg/s, respectively, resulting in an equivalence ratio of 0.833 (equivalent to 20% excess air). Atmospheric pressure is considered for the furnace exhaust. The operating conditions of fuel and air, shaded in Table 2, represent two hydraulic parameters whose effects on furnace performance are investigated in this study. Additionally, convective heat transfer is chosen as the wall boundary condition for the shell body. The internal and external contact surfaces of the coil are individually considered as coupled wall boundary conditions. The properties of the coil material are provided in Table 3.

The solution method is adjusted using the pseudo-transient coupled scheme. Least square cell-based with second-order upwind methods are employed to determine the fluxes in the finite-volume scheme. To ensure a stable numerical solution, the radiation equation is activated only after achieving a well-organized convergence.

5. Validation

To ensure the robustness of the presented results regardless of the computational grid, Fig. 3 illustrates the furnace exhaust temperature for four different grid sizes. It is evident that the temperatures obtained from the third and fourth grids closely align, with only a 6% difference between them. Therefore, based on the error-CPU time tradeoff criterion, the third computational grid containing 3,165,349 elements is selected as the most suitable grid for subsequent numerical simulations. A depiction of this optimal grid is provided in Figs. 4 and 5, along with close-up views of different surfaces.

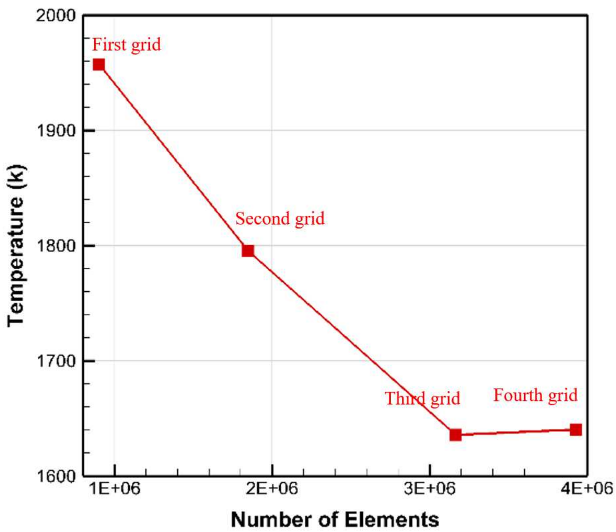

Fig. 3. The results of grid independence study.

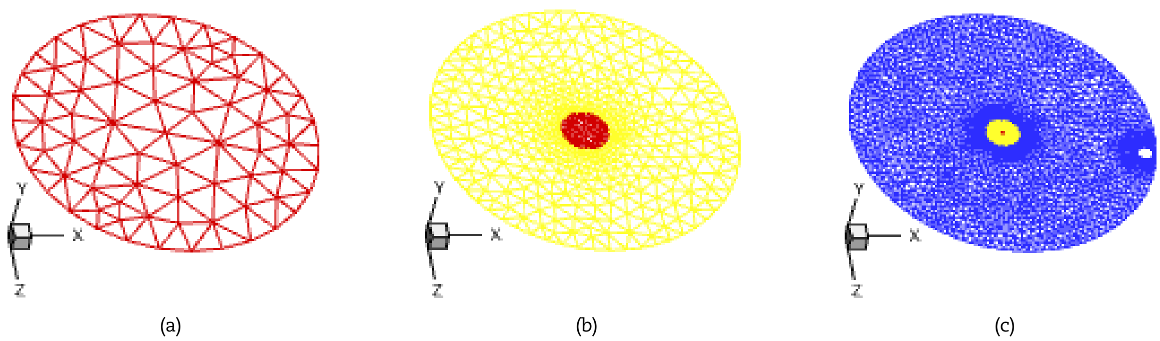

Fig. 4. Representation of different two-dimensional discrete surfaces in the final computational grid, (a) fuel inlet, (b) fuel & air inlets (FAIs), (c) bottom wall & FAIs.

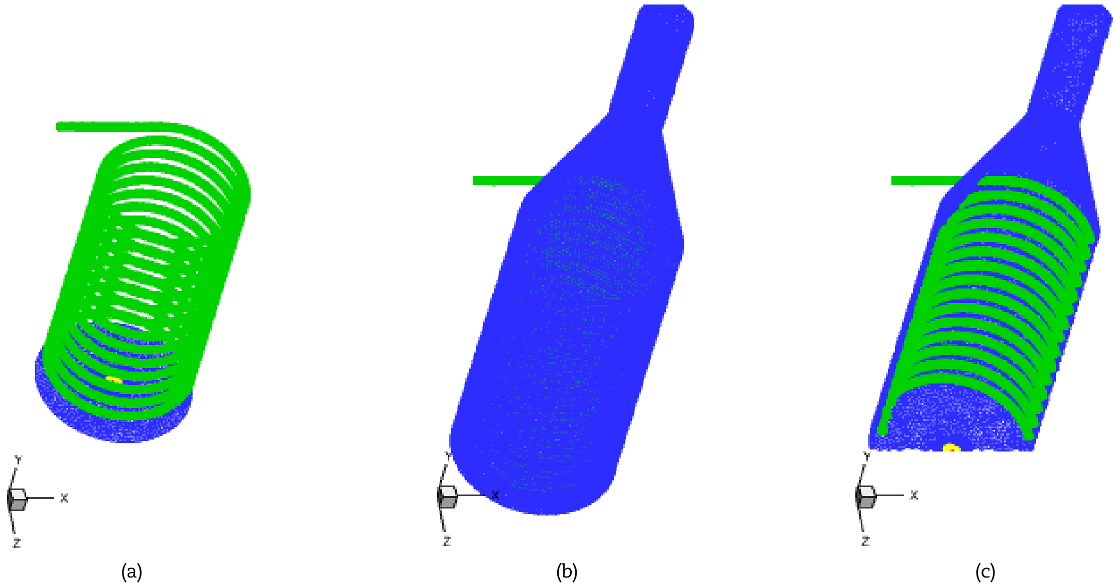

Fig. 5. Representation of different Three-dimensional discrete surfaces in the final computational grid (a) coil and bottom wall & FAIs surfaces, (b) furnace and surfaces, (c) sliced view.

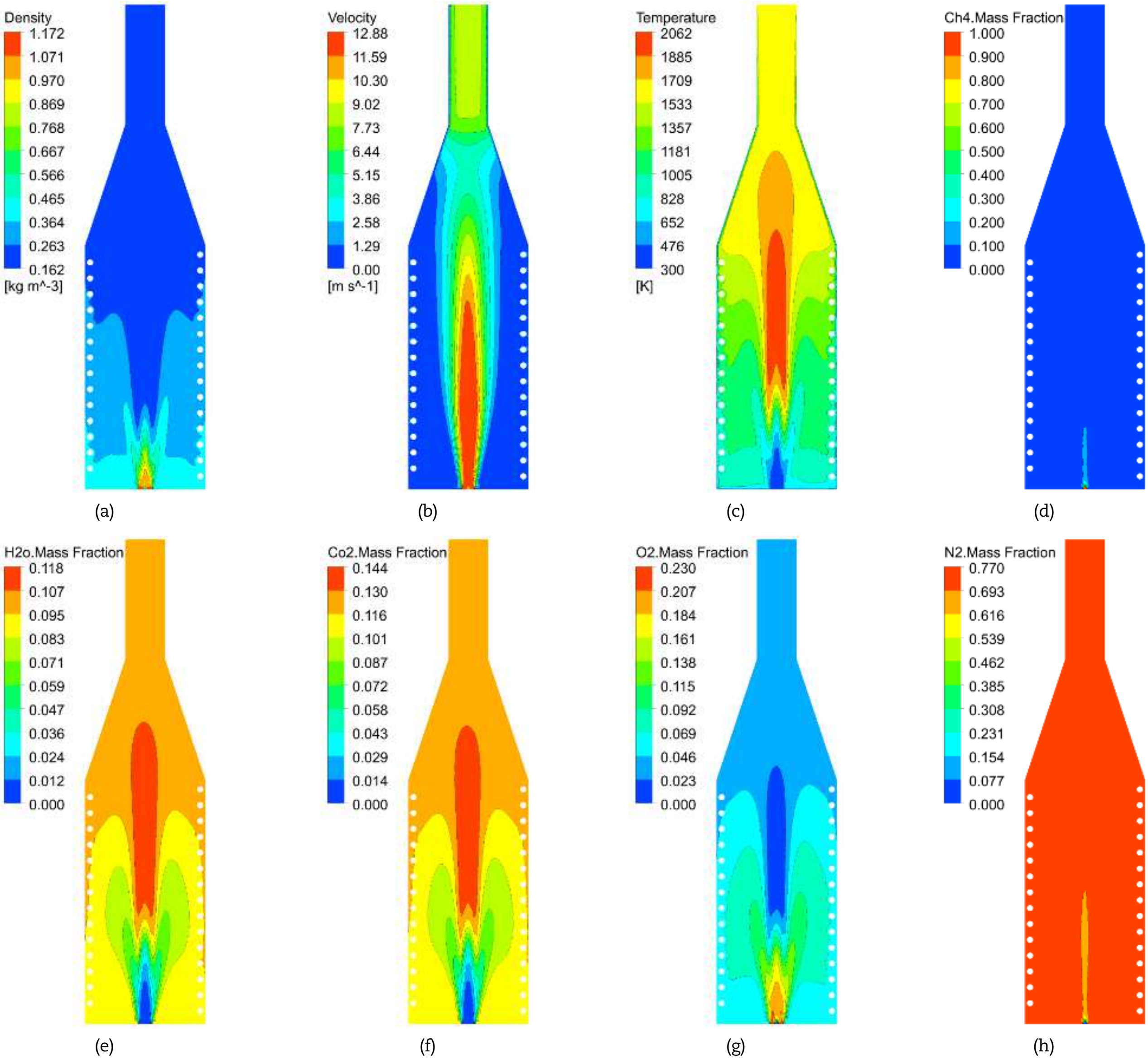

Fig. 6. Contours of the combustion parameters, (a) density, (b) velocity, (c) temperature, (d) CH_4 mass fraction, (e) H_2O mass fraction, (f) CO_2 mass fraction, (g) O_2 mass fraction, (h) N_2 mass fraction.

Table 4. Comparison of outlet ammonia temperature obtained from the numerical solution with the RPC's field data.

Numerical solution (K)	Field data (K)	Relative error (%)
610.146	616.483	1.0

Table 5. List of studied parameters and the range of their changes.

Type	Description	Values	Unit
Hydraulic	Equivalence ratio	0.625, 0.714, 0.833 and 1.0	Dl*
	Fuel mass flow	0.0557, 0.1057 and 0.1557	kg/s
Geometric	Hydraulic diameter of air nozzle	0.23, 0.43 and 0.63	m
	Fuel nozzle diameter	0.05, 0.1 and 0.15	m

* Dl: Dimensionless

Additionally, the outlet ammonia temperature value is compared with the field data from RPC in Table 4. A minimal relative error of 1% indicates a high accuracy of 99% in the numerical simulation results. Furthermore, temperature, velocity, density, and species mass fraction contours are presented in Fig. 6.

6. Parametric Study Results

In this section, we focus on investigating the effects of four parameters on the performance of RPC's ammonia furnace. These parameters are categorized into two types: hydraulic and geometric. Hydraulic parameters include the equivalence ratio and fuel mass flow, while geometric parameters consist of the fuel nozzle diameter and the hydraulic diameter of the air nozzle. Table 5 outlines the variations applied to each parameter, providing insight into the range of changes explored in the study.

6.1. Effect of Equivalence Ratio

In this section, we examine the impact of the equivalence ratio on the combustion process while keeping other parameters constant. Four values of the equivalence ratio are selected: 1.0, 0.833, 0.714, and 0.625, corresponding to 0%, 20%, 40%, and 60% excess air, respectively. The mass flow of injected air under these four equivalence ratios is equivalent to 0.96, 1.15, 1.35, and 1.54 kg/s, respectively. Figure 7(a) depicts the impact of the four equivalence ratios on temperature distribution along the furnace centerline (Y-axis direction in Fig. 1(b)). Although the temperature distribution remains largely consistent for all four ratios until the middle of the spiral coil section, variations emerge along the rest of the furnace height. As the equivalence ratio decreases, the furnace exhaust temperature also decreases. This phenomenon can be attributed to the lower temperature of excess air and its interaction with the air already present inside the furnace. The higher temperature observed at the furnace exhaust for an equivalence ratio of 1.0 is due to the increased time available for mixing the flows inside the furnace. Consequently, the distribution of velocity magnitude along the furnace centerline is illustrated in Fig. 7(b). It is evident that the flow velocity is slower when there is no excess air $(\phi = 1)$ compared to cases with excess air $(\phi < 1)$. This slower velocity allows the fuel more time to remain in the furnace and mix with the air.

The enhanced fuel-air mixing resulting from the increase in flow velocity accelerates the onset and completion of combustion reactions. Consequently, the production of combustion products, such as CO_2 and H_2O, accelerates as well, requiring less furnace height to achieve the desired combustion outcomes. This trend is illustrated in Figs. 8(a) and 8(b). Although the mass fraction distribution of N_2 along the furnace centerline remains unchanged when the reaction is carried out with excess air, some oxygen is released from the furnace shell (see Figs. 8(c) and 8(d)).

It is noticeable that as the equivalence ratio decreases, the amount of oxygen leaving the combustion chamber increases. When the reaction is conducted with theoretical air (no excess air), all the oxygen is consumed inside the furnace (see Fig. 9).

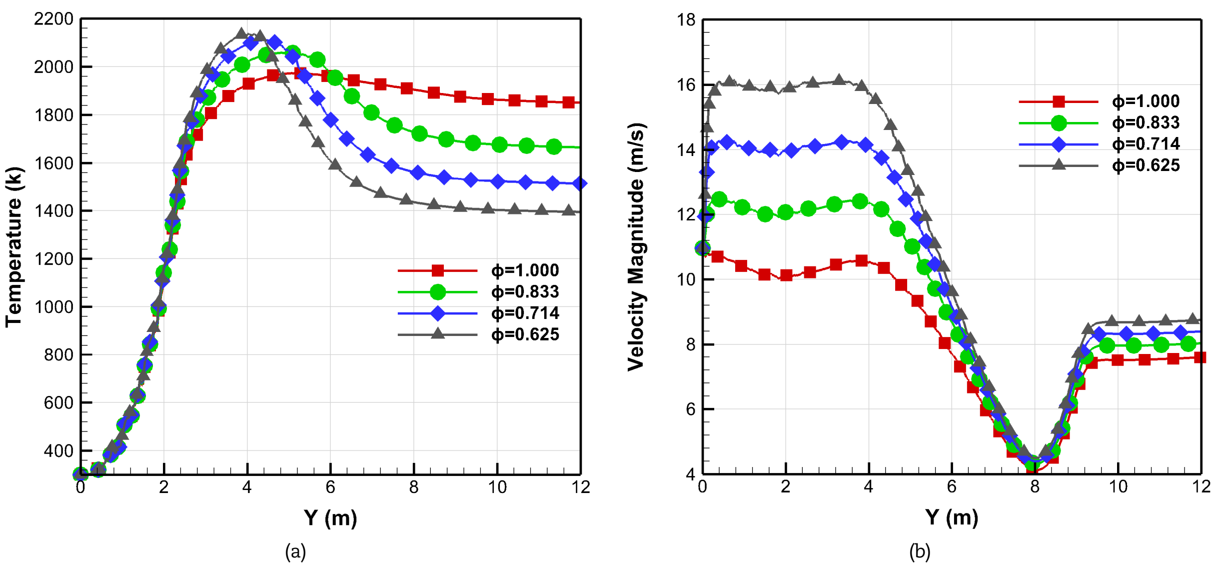

Fig. 7. Distribution of flow parameters inside furnace for different equivalence ratios, (a) Temperature, (b) Velocity.

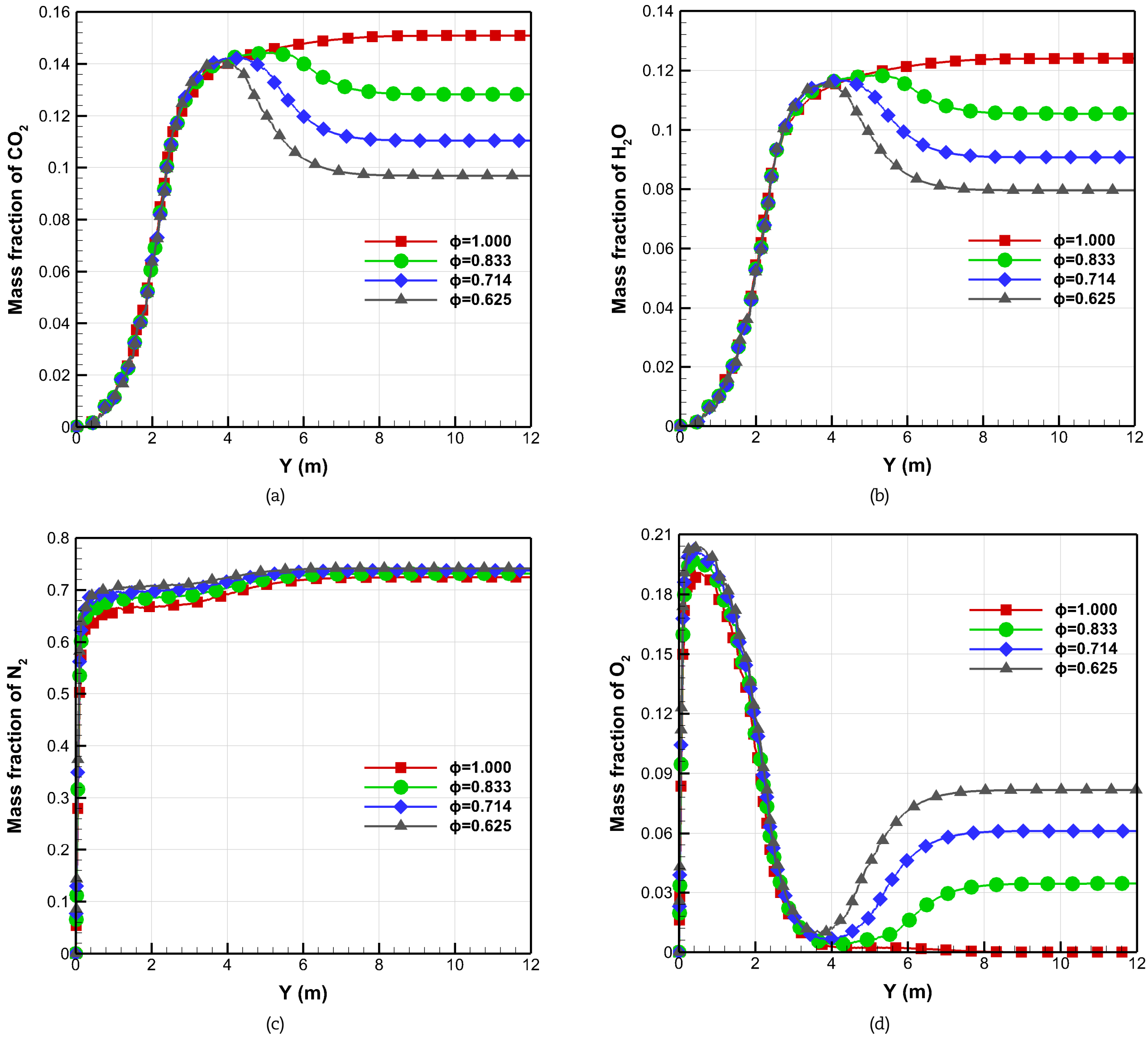

Fig. 8. Mass fraction of combustion species for different equivalence ratios, (a) CO_2, (b) H_2O, (c) O_2, (d) N_2.

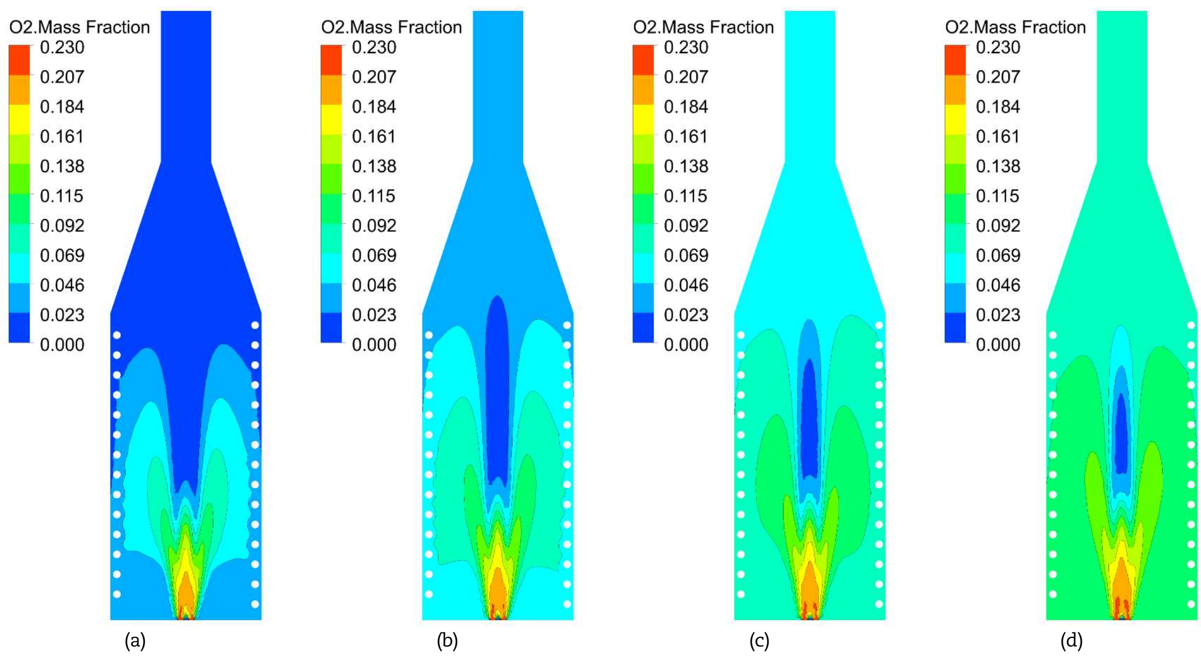

Fig. 9. Contour plots of equivalence ratio effect on the O_2 mass fraction, (a) ϕ = 1.000, (b) ϕ = 0.833, (c) ϕ = 0.714, (d) ϕ = 0.625.

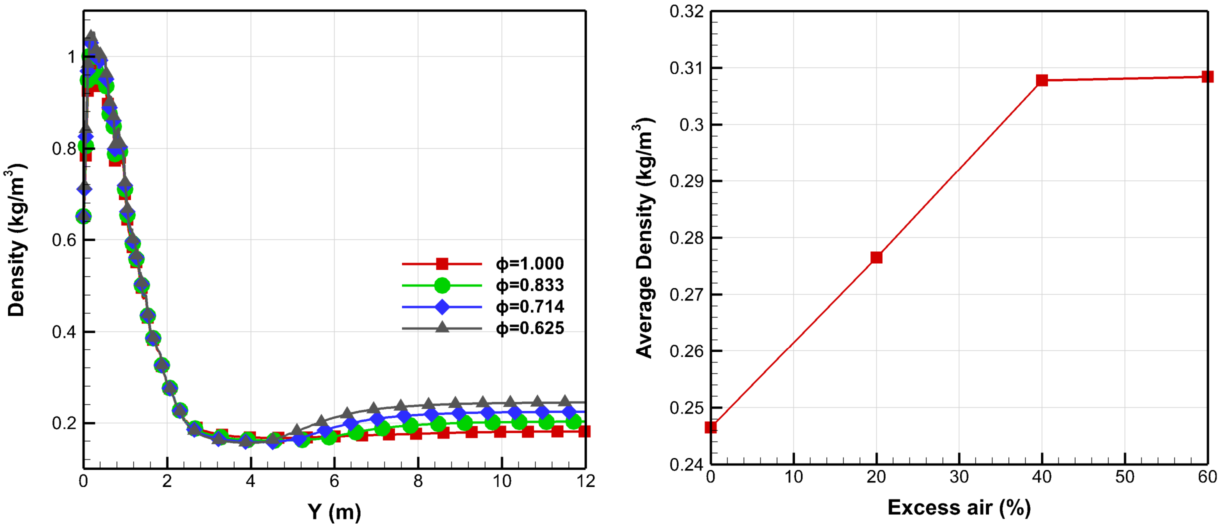

Fig. 10. Density distribution along the furnace centerline and in light of the excess air, (a) Local Density, (b) Average Density.

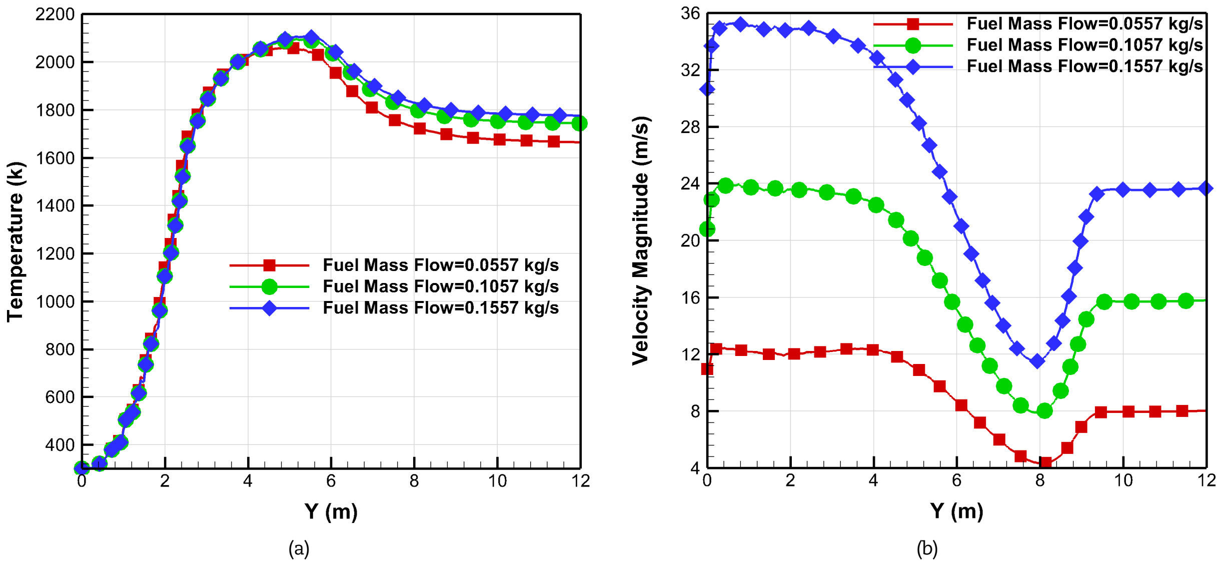

Fig. 11. Distribution of flow parameters inside furnace for different fuel mass flow, (a) Temperature, (b) Velocity.

This phenomenon can also impact the flow density distribution, as depicted in Fig. 10(a). Furthermore, Fig. 10(b) illustrates that the average flow density is directly correlated with excess air. The increase in average density is attributed to the higher density of air compared to methane gas.

6.2. Effect of Fuel Mass Flow

In this section, the results for the fuel mass flows of 0.0557, 0.1057, and 0.1557 kg/s, corresponding to air mass flows of 1.15, 2.19, and 3.22 kg/s to maintain a 20% excess air condition, are presented. Figure 11(a) displays the temperature distribution inside the furnace. It's observed that with an increase in fuel mass flow, the maximum temperature inside the furnace rises due to the elevation in flow velocity (see Fig. 11(b)). This temperature rise occurs while keeping the fuel nozzle diameter and the hydraulic diameter of the air nozzle unchanged.

As demonstrated in this section, the increase in air mass flow is directly correlated with the rise in fuel mass flow. Consequently, the combustion reaction rates remain consistent across different fuel mass flows. This consistency results in similar mass fraction distributions of all reaction species at different fuel mass flows, as depicted in Fig. 12.

6.3. Effect of Air Hydraulic Diameter

In this section, we present the results corresponding to air hydraulic diameters of 0.23, 0.43, and 0.63 m. Figure 13(a) illustrates the impact of different air hydraulic diameters on temperature distribution. Upon examination of the results, it becomes evident that the air velocity is higher when the hydraulic diameter of the incoming air is smaller (see Fig. 13(b)). In such cases, the fuel and air mix more effectively, leading to combustion reactions occurring at a shorter distance from the burner. Consequently, the temperature distribution becomes more uniform along the rest of the furnace centerline length.

In Fig. 14, we observe how changes in the air hydraulic diameter impact the mass fraction of combustion species. With consistent fuel and air flow rates across all scenarios, we find that for hydraulic diameters of 0.23 and 0.43 meters, the generation of combustion products remains closely aligned, differing only in their attributed products across various sections within the furnace. However, this pattern deviates from the 0.63-meter diameter, where incomplete combustion reaction occurs within the furnace.

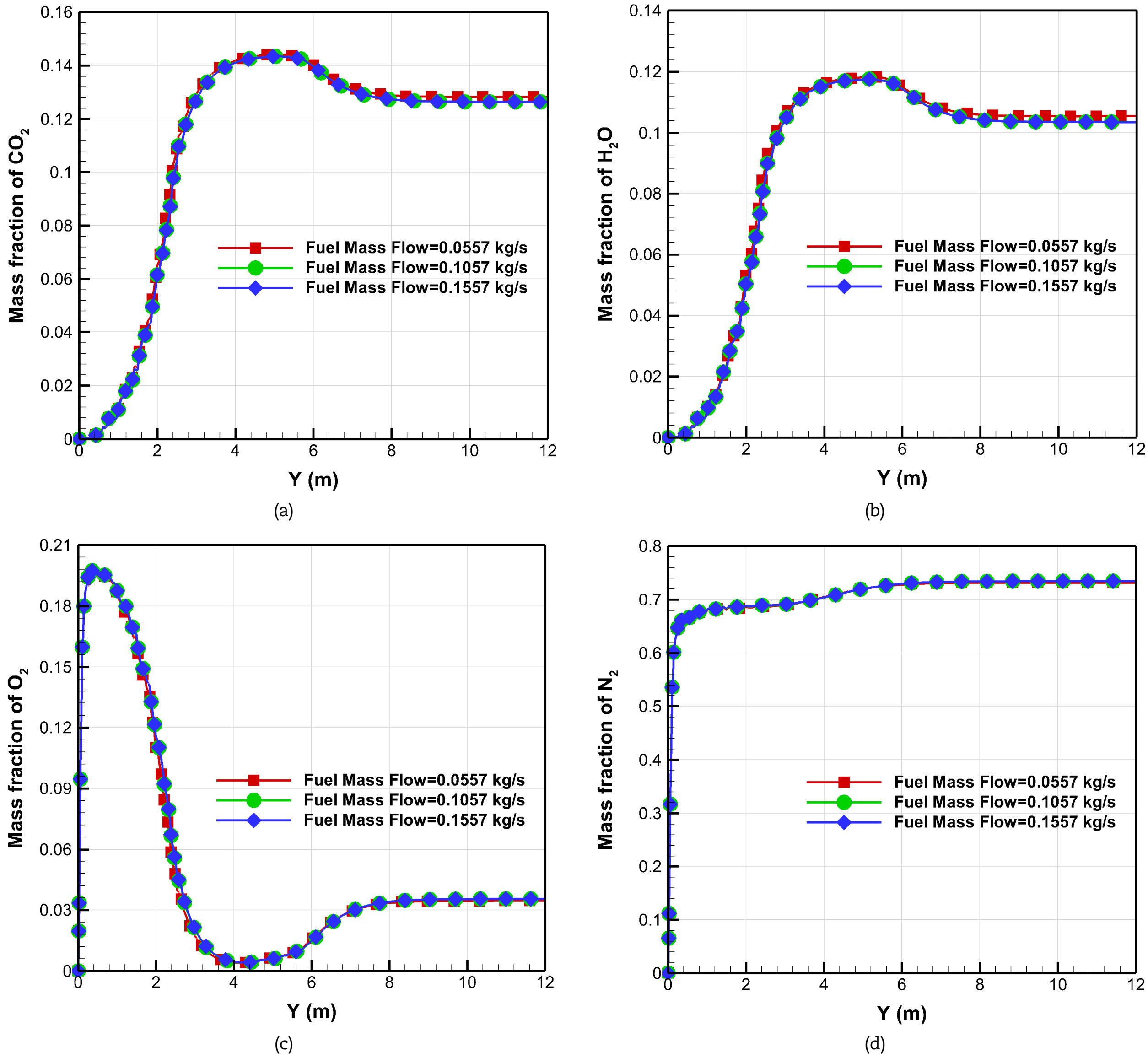

Fig. 12. Effect of the different fuel mass flow on the combustion parameters, (a) CO_2, (b) H_2O, (c) O_2, (d) N_2.

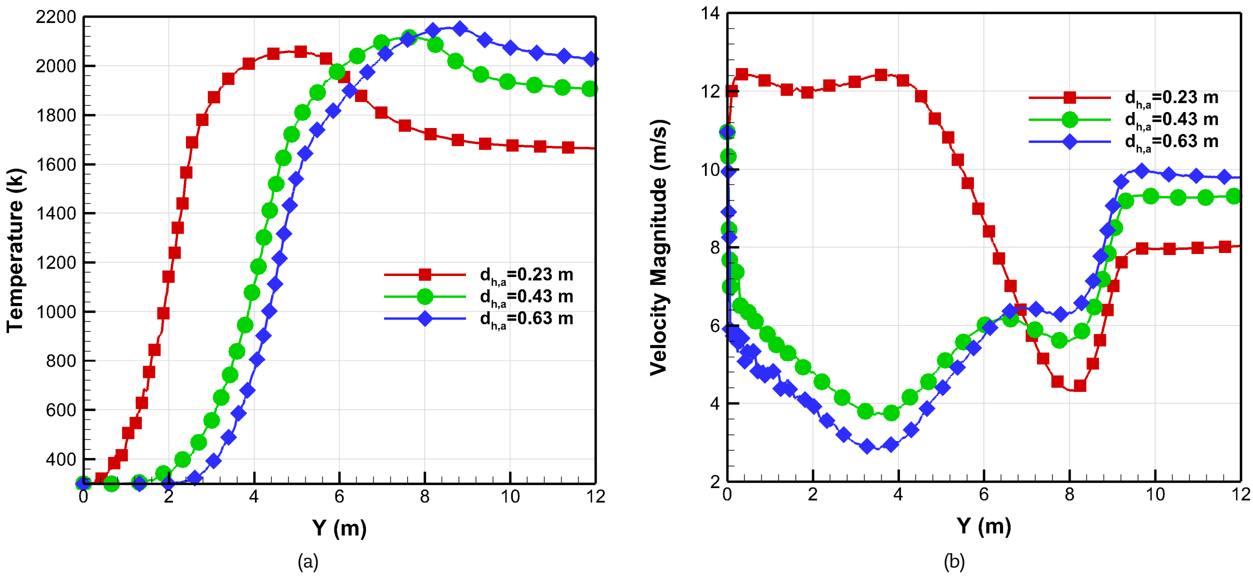

Fig. 13. Distribution of flow parameters inside furnace for different air hydraulic diameters, (a) Temperature, (b) Velocity.

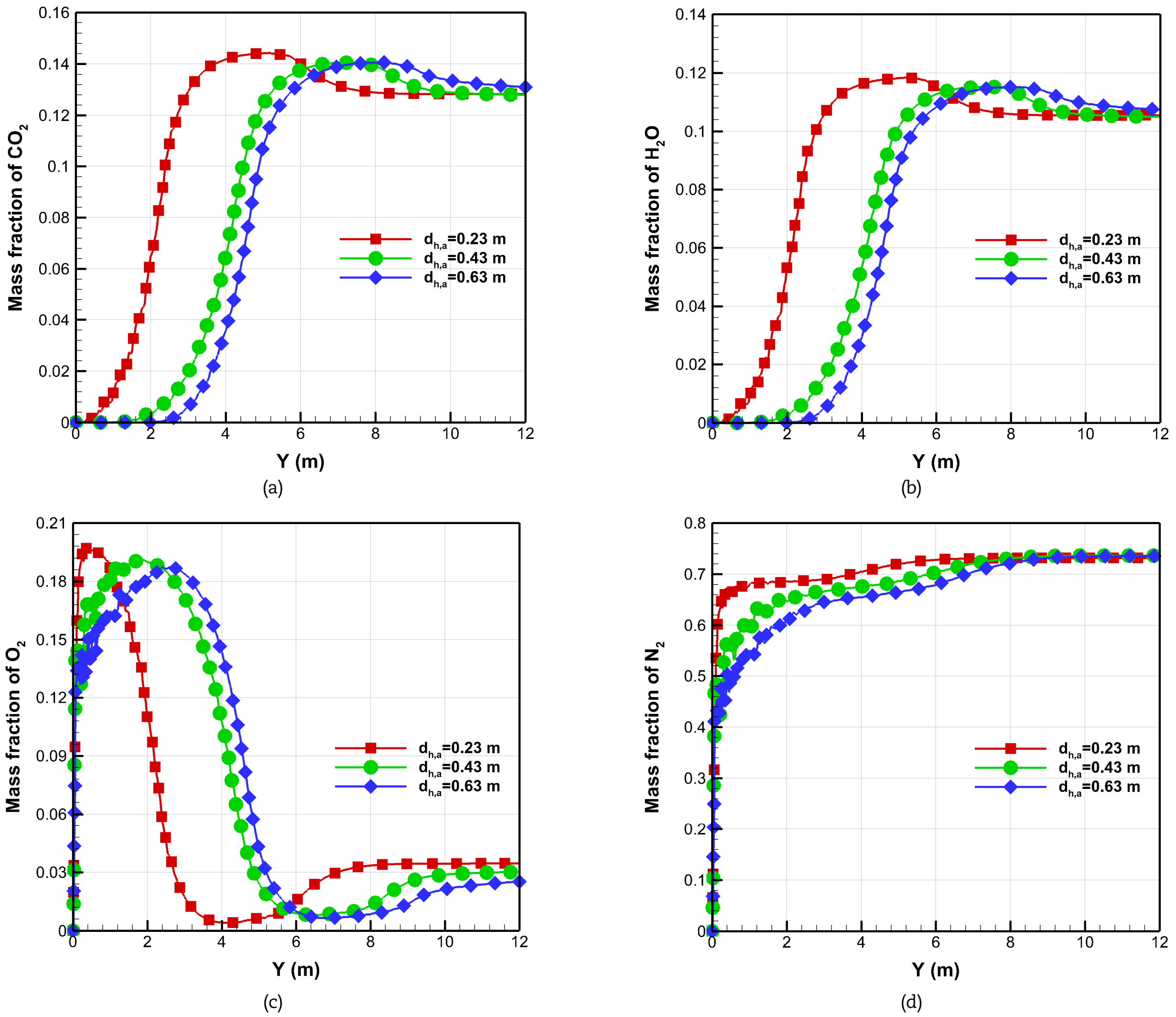

Fig. 14. Effect of the different air hydraulic diameters on the combustion parameters, (a) CO_2, (b) H_2O, (c) O_2, (d) N_2.

As depicted in Figs. 13(b) and 14, lower incoming air velocities (associated with larger hydraulic diameters) result in slower combustion product production at the furnace's initial sections. Conversely, closer to the exhaust, combustion product production increases. Conversely, higher air speeds (linked to smaller hydraulic diameters) exhibit the opposite trend. This variation can be attributed to the flame formation location. Higher air velocities facilitate better mixing of fuel and air, leading to flame formation closer to the bottom of the shell. Consequently, the reaction initiates and concludes more swiftly, accelerating product production and requiring less shell height. In Fig. 14(d), excess oxygen release at the furnace exhaust is observed due to the combustion occurring with surplus air at the smallest hydraulic diameter. Oxygen consumption increases with higher air velocity until the reaction reaches completion, at which point excess oxygen escapes from the furnace exhaust.

6.4. Effect of Fuel Nozzle Diameter

We consider three fuel nozzle diameters: 0.05, 0.1, and 0.15 meters, alongside a constant outer diameter of 0.33 meters for the incoming air nozzle. Consequently, the hydraulic diameters for the air nozzle are computed as 0.28, 0.23, and 0.18 meters, respectively. It is evident that increasing the diameter of the fuel inlet nozzle results in a decrease in the hydraulic diameter of the air nozzle. This suggests a reduction in velocity for injected fuel and an increase in injected air. Higher air velocities enhance the mixing of fuel and air. Temperature distribution and velocity magnitude plots for different fuel nozzle diameters are presented in Figure 15. The analysis of the results in this section aligns with that of the previous section.

7. Discussion

In this section, we delve into the impact of the studied hydraulic and geometric parameters on furnace performance, with a focus on heat transfer rate and pollutant emissions as key indicators. Figure 16(a) illustrates how excess air affects the rate of heat transferred to the ammonia vapor. With increasing excess air, the fluid has less time to transfer heat to the coil due to the accelerated flow velocity. Consequently, the temperature difference between the fluid flow and the coil surface diminishes. However, the convective heat transfer coefficient rises with the increase in flow velocity. Nonetheless, the reduction in temperature difference outweighs the increase in the convective heat transfer coefficient, leading to a decrease in the rate of heat exchanged with the coil, down to 357 kW with each increment in excess air. Figure 16(b) demonstrates a direct correlation between pollutant emissions and excess air. As depicted in Fig. 7(a), the maximum temperature reaches 2143 K with the rise in excess air magnitude. The highest concentration of pollutants corresponds to the highest combustion temperature. Thus, pollutant emissions increase to 165 ppm with the elevation of excess air. Overall, the findings from the excess air study suggest that a 20% excess air condition is optimal for operating the RPC's furnace.

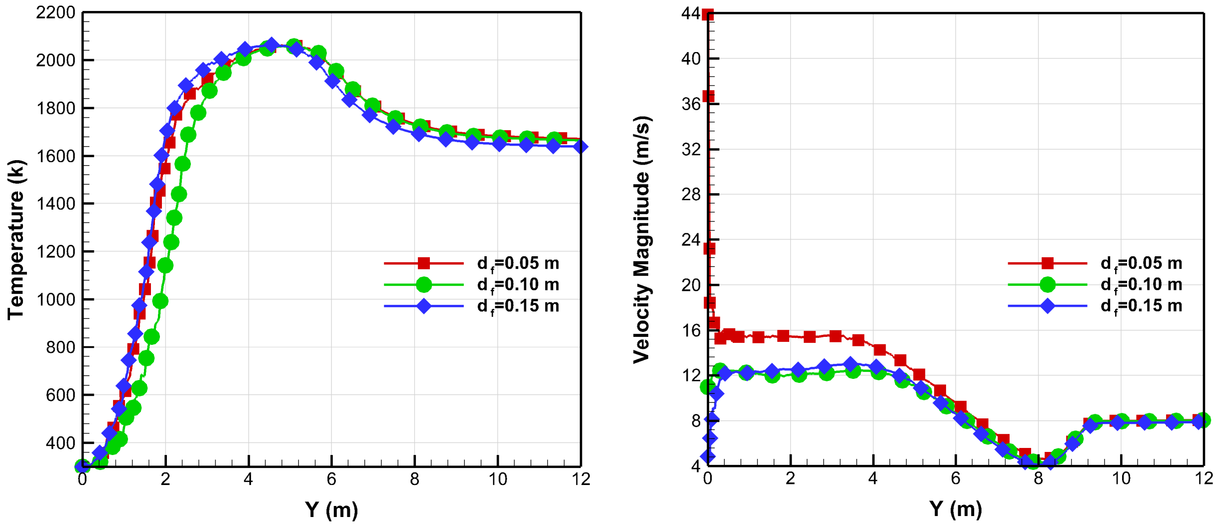

(a) (b)

Fig. 15. Distribution of flow parameters inside furnace for different air hydraulic diameters, (a) Temperature, (b) Velocity.

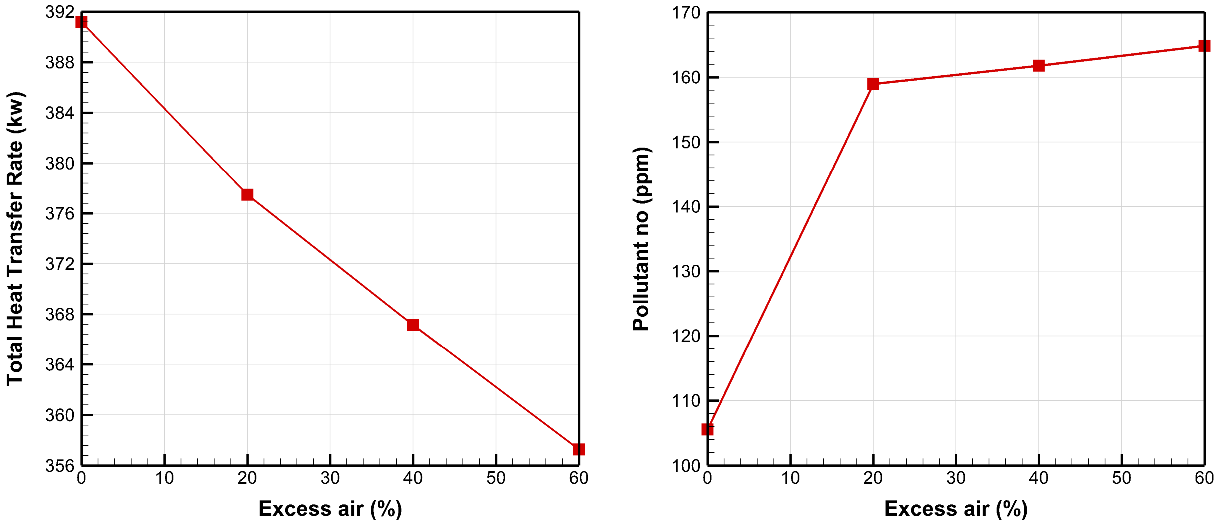

(a) (b)

Fig. 16. Effect of the excess air on the furnace performance, (a) Heat transfer rate, (b) Pollutants emission.

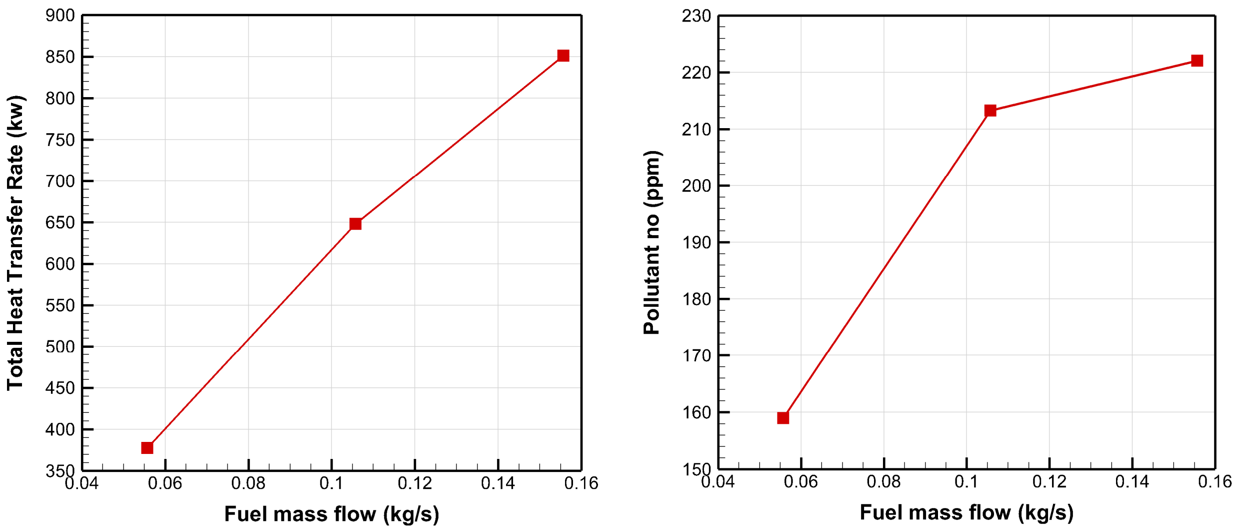

(a) (b)

Fig. 17. Effect of the fuel mass flow on the furnace performance, (a) Heat transfer rate, (b) Pollutants emission.

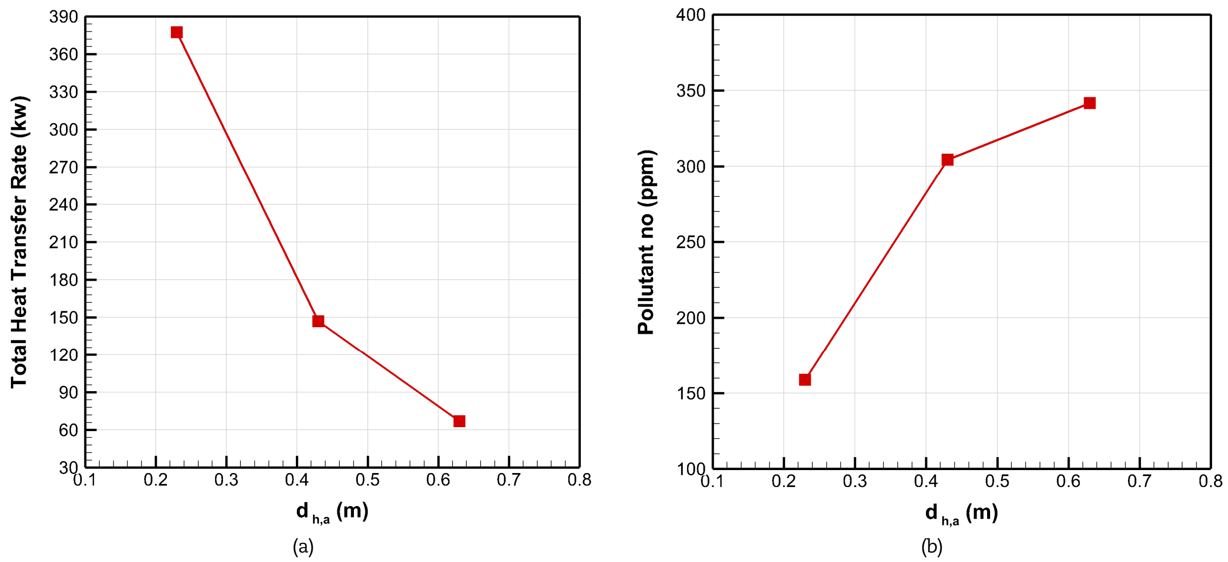

Fig. 18. Effect of the air hydraulic diameter on the furnace performance, (a) Heat transfer rate, (b) Pollutants emission.

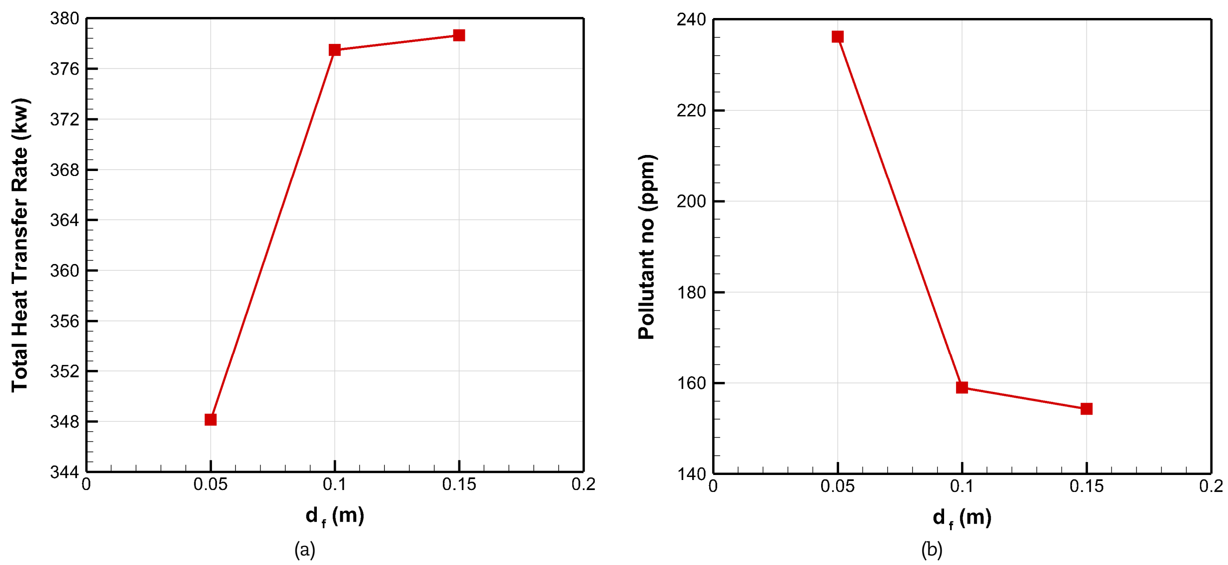

Fig. 19. Effect of the fuel nozzle diameter on the furnace performance, (a) Heat transfer rate, (b) Pollutants emission.

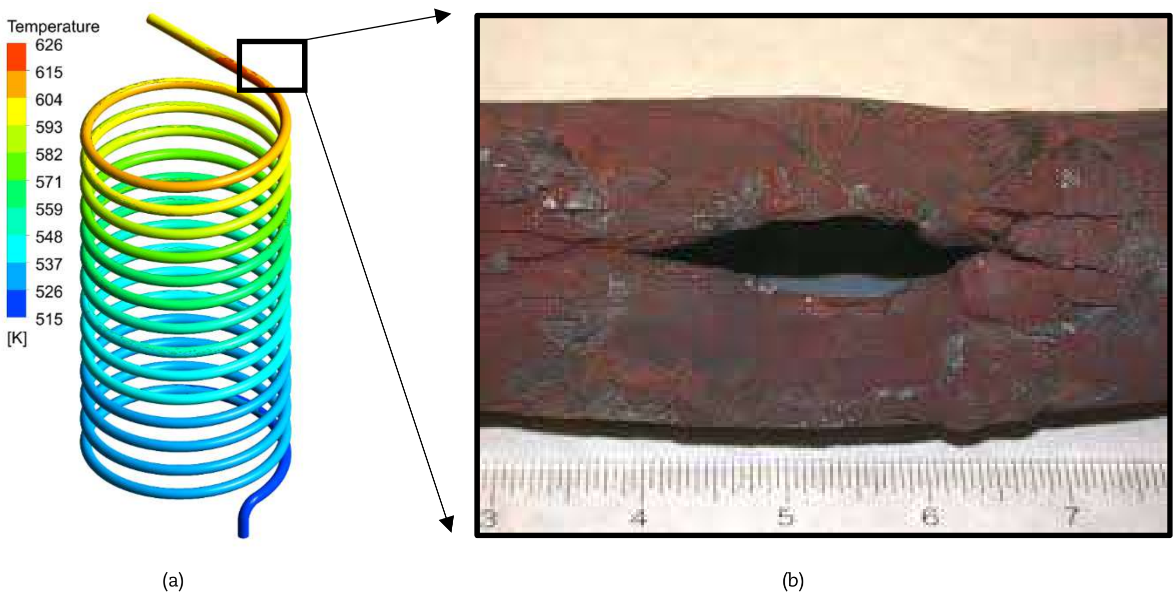

Fig. 20. Representation of the hot spot location and its situation on the realistic coil surface, (a) Temperature distribution, (b) Realistic exhibition.

Another critical parameter influencing combustion within the furnace is the fuel mass flow rate. Figure 17(a) delves into the effect of changes in fuel mass flow rate on the rate of heat transferred to ammonia. As the fuel mass flow increases, the rate of heat exchanged with the coil rises to 850 kW due to enhanced combustion resulting from burning more fuel. Figure 17(b) illustrates that increasing fuel flow leads to a rise in pollutant emissions, reaching 222 ppm. This trend aligns with the principle that pollutant emissions escalate with temperature increments. Additionally, the maximum furnace temperature increases with higher fuel flow rates. In summary, the outcomes of our analysis affirm that a fuel mass flow rate of 0.1 kg/s represents a balanced choice, effectively optimizing the trade-off between heat transfer rate and pollutant emissions.

Figure 18 illustrates the impact of the air hydraulic diameter on the rate of heat transferred to ammonia. It is observed that the heat transfer rate decreases almost monotonically with an increase in the diameter of the incoming air. This phenomenon can be attributed to the location of the flame (as depicted by the maximum temperature in Fig. 13(a)). As the hydraulic diameter increases, the flame forms at a greater distance from the burner, leading to a decrease in the heat transfer rate. Similar to the interpretation of Fig. 17(b), the magnitude of pollutant emissions rises with increasing air hydraulic diameter. Considering the trade-off between heat transfer rate and pollutant emissions, a hydraulic diameter of 0.23 m emerges as the optimal design for the incoming air nozzle. Analogously, the results presented in Fig. 19 demonstrate that a fuel nozzle diameter of 0.1 m effectively delivers adequate heat to the coil surface while controlling pollutant emissions at a proper level.

Despite achieving optimal parameter values as outlined in Table 1 for geometric conditions and Table 2 for hydraulic conditions, a persistent issue remains with this furnace: the occurrence of hot spots on the coil surface. Typically, these hot spots manifest at the topmost section of the coil. In addressing this concern, we present the temperature distribution of the coil surface, incorporating parameters from Tables 1 and 2, in Fig. 20. This visualization accurately depicts the presence of hot spots, exemplified by the realistic portrayal of a localized hole. Notably, the maximum thermal stress is concentrated at the end length of the coil. The formation of hot spots on the coil poses significant challenges, imposing substantial costs for maintenance and repair within the RPC facility. In this paper, the thermal stress on the coil is linked to the maximum temperature, which decreases with increasing excess air, thereby reducing the likelihood of tube perforation and hot spots. Conversely, increasing the fuel flow rate raises the maximum temperature due to higher fuel and air speeds, increasing the risk of tube puncture. Additionally, reducing the hydrodynamic diameter of the air inlet enhances fuel-air mixing, resulting in a higher maximum flame temperature within a smaller range. To address the recurrent maintenance issues at the end of the coil, one potential solution could be the use of more heat-resistant materials for the coil. Advanced alloys or ceramic coatings might offer improved durability and resistance to thermal stress. Moreover, optimizing the cooling mechanisms and implementing better thermal management strategies could also help mitigate these issues. These approaches could enhance the longevity of the coil and reduce the frequency of maintenance.

8. Conclusions

This study presented a numerical analysis of the combustion process within the RPC's preheating ammonia furnace. Through geometrical modeling and fluid flow simulations, our findings revealed a noteworthy correlation between exhaust temperature and the introduction of low-temperature excess air, coupled with its mixing within the furnace. The results showed that with an increase in the percentage of excess air, the furnace outlet temperature and the likelihood of tube perforation decrease due to the reduction in maximum coil temperature. Additionally, while the exhaust temperature decreases with excess air addition, there is a concurrent increase in fluid flow velocity within the furnace. The presence of excess air confines combustion to a more delimited area, resulting in higher temperatures concentrated at the flame's center, a shortened flame length, and fewer combustion products. Despite the substantial oxygen consumption at higher air velocities, this consumption diminishes along the furnace centerline until combustion reaction completion, with excess oxygen subsequently released from the exhaust. Furthermore, increasing the fuel flow rate raises the maximum temperature and the risk of tube perforation, while reducing the air hydraulic diameter promotes better fuel-air mixing, resulting in a more confined range for maximum flame temperature. Our results indicate that the highest emissions of pollutants correspond to cases with the highest combustion temperatures. The production of NOx pollutants increases exponentially with higher maximum temperatures, thus increasing the air inlet diameter, fuel flow rate, and percentage of excess air results in higher NOx emissions. These findings suggest that proper adjustment of these variables can enhance furnace efficiency and reduce pollutants.

Author Contributions

The authors confirmed the contributions to this article as follows: Alireza Daneh-Dezfuli: Original draft and supervision. Shiva Khamisi: Review and conceptualization. Seyed Saied Bahrainian: Review and editing. The manuscript was written through the contribution of all authors. All authors discussed the results, reviewed, and approved the final version of the manuscript.

Acknowledgments

Not Applicable.

Conflict of Interest

The authors declared that they have no conflict of interest.

Funding

This work was supported by Shahid Chamran University of Ahvaz under Grant No. SCU.EM1403.26639.

Data Availability Statements

Not Applicable.

References

[1] Silva Neto, G.C., Chui, D.S., Martins, F.P., Fleury, A.T., Furnari, F., Trigo, F.C., Identification of CO2 and O2 emissions dynamics in a natural gas furnace through flame images, ARMAX models, and Kalman filtering, *Journal of the Brazilian Society of Mechanical Sciences Engineering*, 43(5), 2021, 256.

[2] Jia, Y., Zhou, W., Tang, J., Luo, Y., Design optimization and CFD evaluation of a volute swirl burner with central gas supply, *Journal of the Brazilian Society of Mechanical Sciences Engineering*, 42(4), 2020, 196.
[3] Mancini, M., Weber, R., Bollettini, U., Predicting NOx emissions of a burner operated in flameless oxidation mode, *Proceedings of the Combustion Institute*, 29(1), 2002, 1155-1163.
[4] Yapıcı, H., Kayatas, N., Albayrak, B., Basturk, G., Numerical calculation of local entropy generation in a methane–air burner, *Energy Conversion and Management*, 46(11-12), 2005, 1885-1919.
[5] Saario, A., Rebola, A., Coelho, P., Costa, M., Oksanen, A., Heavy fuel oil combustion in a cylindrical laboratory furnace: measurements and modeling, *Fuel*, 84(4), 2005, 359-369.
[6] Yang, W., Blasiak, W., Numerical study of fuel temperature influence on single gas jet combustion in highly preheated and oxygen deficient air, *Energy*, 30(2-4), 2005, 385-398.
[7] Vuthaluru, R., Vuthaluru, H., Modelling of a wall fired furnace for different operating conditions using FLUENT, *Fuel Processing Technology*, 87(7), 2006, 633-639.
[8] Schaffel-Mancini, N., Mancini, M., Szlek, A., Weber, R., Novel conceptual design of a supercritical pulverized coal boiler utilizing high temperature air combustion (HTAC) technology, *Energy*, 35(7), 2010, 2752-2760.
[9] Huang, M.-M., Shao, W.-W., Xiong, Y., Liu, Y., Zhang, Z.-D., Lei, F.-L., Xiao, Y.-H., Effect of fuel injection velocity on MILD combustion of syngas in axially-staged combustor, *Applied Thermal Engineering*, 66(1-2), 2014, 485-492.
[10] He, Y., Zou, C., Song, Y., Liu, Y., Zheng, C., Numerical study of characteristics on NO formation in methane MILD combustion with simultaneously hot and diluted oxidant and fuel (HDO/HDF), *Energy*, 112, 2016, 1024-1035.
[11] Elorf, A., Sarh, B., Excess air ratio effects on flow and combustion caracteristics of pulverized biomass (olive cake), *Case Studies in Thermal Engineering*, 13, 2019, 100367.
[12] Tu, Y., Xu, S., Xie, M., Wang, Z., Liu, H., Numerical simulation of propane MILD combustion in a lab-scale cylindrical furnace, *Fuel*, 290, 2021, 119858.
[13] Ceglie, V., Stefanizzi, M., Capurso, T., Fornarelli, F., Camporeale, S.M., Thermoacoustic Combustion Stability Analysis of a Bluff Body-Stabilized Burner Fueled by Methane–Air and Hydrogen–Air Mixtures, *Energies*, 16(7), 2023, 3272.
[14] Cao, J., Sun, Y., Yang, F., Zhao, X., Gu, Y., Tan, H., Experimental and Numerical Study on the Combustion Characteristics of Premixed Methane/Air in Porous Media Burner, *Combustion Science and Technology*, 2024, https://doi.org/10.1080/00102202.2024.2340724.
[15] Sun, M., Shao, Y., Gong, Y., Xu, C., Song, T., Lu, P., Agarwal, R.K., Numerical Investigation of Flow and Flame Structures in an Industrial Swirling Inverse Diffusion Methane/Air Burner, *Fire*, 7(7), 2024, 237.
[16] Dekhatawala, A., Bhale, P., Shah, R., Effect of Equivalence Ratio on Flame Morphology, Thermal and Emissions Characteristics of Inverse Diffusion Porous Burner, *Journal of Applied Fluid Mechanics*, 17(6), 2024, 1217-1229.
[17] Liao, M., He, Z., Jia, S., Liang, X., Chan, T.L., Li, Y., Xu, X., Liu, T., Comparison of the flame stabilities during oxy-methane and air-methane combustion in a two-layer porous burner, *Case Studies in Thermal Engineering*, 51, 2023, 103657.
[18] Hulsbos, M.R., Hermanns, R.T.E., Bastiaans, R.J.M., de Goey, L.P.H., The Heat Flux Method for hybrid iron–methane–air flames, *Combustion and Flame*, 266, 2024, 113531.
[19] Füzesi, D., Wang, S., Józsa, V., Chong, C.T., Ammonia-methane combustion in a swirl burner: Experimental analysis and numerical modeling with Flamelet Generated Manifold model, *Fuel*, 341, 2023, 127403.
[20] Al-Khafaji, M., Yang, J., Tomlin, A.S., Thompson, H.M., de Boer, G., Liu, K., Morsy, M.E., Laminar burning velocities and Markstein numbers for pure hydrogen and methane/hydrogen/air mixtures at elevated pressures, *Fuel*, 354, 2023, 129331.
[21] Fluent, A., *Ansys fluent theory guide*, ANSYS Inc., USA, 2018.
[22] White, F.M., Corfield, I., *Viscous fluid flow*, McGraw-Hill, New York, 2006.
[23] Incropera, F.P., DeWitt, D.P., Bergman, T.L., Lavine, A.S., *Fundamentals of heat and mass transfer*, Wiley, New York, 1996.
[24] Cengel, Y.A., Boles, M.A., *Thermodynamics: An Engineering Approach 6th Editon (SI Units)*, The McGraw-Hill Companies, Inc., New York, 2007.
[25] Siswantara, A.I., Darmawan, S., Tanujaya, H., Inverse-turbulent Prandtl number effects on Reynolds numbers of RNG k-ε turbulence model on cylindrical-curved pipe, *Applied Mechanics and Materials*, 758, 2015, 35-44.
[26] Yan, S., Tang, G., Zhou, C.Q., Guo, X., Computational Fluid Dynamics Modeling of Combustion Characteristics of a CH4/O2 Combustor in a Copper Anode Furnace, *ACS Omega*, 4(7), 2019, 12449-12458.
[27] Yang, X., Clements, A., Szuhánszki, J., Huang, X., Moguel, O.F., Li, J., Gibbins, J., Liu, Z., Zheng, C., Ingham, D., Prediction of the radiative heat transfer in small and large scale oxy-coal furnaces, *Applied Energy*, 211, 2018, 523-537.
[28] Jiang, B., Liang, H., Huang, G., Xingang, L., Study on NOx formation in CH4/Air jet combustion, *Chinese Journal of Chemical Engineering*, 14(6), 2006, 723-728.

ORCID iD

Alireza Daneh-Dezfuli https://orcid.org/0000-0002-6082-4189
Seyed Saied Bahrainian https://orcid.org/0000-0001-9783-1326

How to cite this article: Daneh-Dezfuli A., Khamisi S., Bahrainian S.S. Numerical Analysis of Preheating Furnace Performance in Razi Petrochemical's Ammonia Processing Unit Considering the Effects of Hydraulic and Geometric Variables, *J. Appl. Comput. Mech.*, 11(2), 2025, 502-518. https://doi.org/10.22055/jacm.2024.46917.4624